Microturbulence in DIII-D tokamak pedestal. II. Electromagnetic instabilities

I. Holod, D. Fulton and Z. Lin

Department of Physics and Astronomy, University of California, Irvine, CA 92697, USA

E-mail: iholod@uci.edu

CrossMark

Abstract

Gyrokinetic simulations have been used to identify electromagnetic microinstabilities in the H-mode pedestal region of DIII-D shot 131 997 using global gyrokinetic code GTC. It was found that dominant instability at the top of the pedestal is the ion temperature gradient mode (ITG). In the maximum gradient location the most unstable mode is the kinetic ballooning mode (KBM) for the dominant poloidal wavenumber $k_\theta \approx 1\,\mathrm{cm}^{-1}$. For shorter wavelengths the dominant instability is the trapped-electron mode (TEM). We have demonstrated the ITG–KBM transition at the pedestal top, and TEM–KBM transition in the steep pressure gradient region as plasma pressure increases while gradients remain unchanged.

(Some figures may appear in colour only in the online journal)

1. Introduction

Stability and performance of tokamak H-mode operation is crucially dependent on characteristics of plasma pedestal, thus predicting pedestal hight and width is essential for optimizing fusion devices. Due to large pressure and current gradients, pedestal is subject to dangerous magneto-hydrodynamic instabilities, referred to as edge localized modes (ELM). These instabilities cause a partial collapse of the pedestal profiles, accompanied by significant heat and particle fluxes to material surfaces, which may lead to significant erosion of plasma facing materials on reactor-scale devices.

According to experimental observations [1] and EPED model [2], which successfully predicts pedestal pressure profile in many tokamak discharges, the onset of ELM is associated with non-local peeling-ballooning instability at low to intermediate mode number. One possibility to control drastic ELM activity is applying resonant magnetic perturbations (RMP) [3], however, their inward penetration mechanism and effect on transport is not quite clear yet.

Another constraint, which limits pedestal buildup, is the nearly-local kinetic ballooning mode (KBM) with high toroidal mode number. Even though EPED prediction of pedestal profile is reasonably good, it is important to validate the infinite-n MHD local calculation of KBM instability threshold using more realistic gyrokinetic simulation in real tokamak geometry. Although KBM is the prominent candidate for driving turbulent transport in the pedestal [4], other candidates, including micro-scale drift-wave modes, should also be investigated, as these instabilities can limit allowable gradients in the pedestal.

Previous gyrokinetic studies of the H-mode pedestal [5–8] are not conclusive regarding destabilization of KBM, although it was found that the results are particularly sensitive to the geometry model [6] and non-locality [9]. The local flux-tube simulation models rely on the assumption that $k_\perp L_\mathrm{p} \gg 1$, where $k_\perp$ is the perpendicular wavenumber, and L_p is the pressure gradient scale length. While the local assumption can be mostly justified at the top of pedestal where $k_\perp L_\mathrm{p} \sim 25$, it is not strictly applicable in the steep gradient region, where $k_\perp L_\mathrm{p} \sim 5$, assuming $k_\perp \rho_i \approx 1$ where ρ_c is the ion gyroradius. This signifies the importance of using the non-local model for plasma pedestal simulations.

Our previous electrostatic simulations of the DIII-D H-mode pedestal [9] using global gyrokinetic toroidal code GTC [10] with realistic equilibrium [11] from EFIT [12] and VMEC [13] are in general agreement with electrostatic results reported in [5]. In this study, we continue to explore linear instabilities in the H-mode pedestal region using electromagnetic gyrokinetic simulations of the same DIII-D discharge #131997 at time 3011 ms. [14].

Electromagnetic capability in GTC is implemented by using the fluid-kinetic hybrid electron model [15] based on the separation of the electron response into adiabatic and non-adiabatic parts. In the lowest order in $\omega/k_\parallel v_e$ expansion the adiabatic part is approximated by massless fluid response, while in the higher order it is adjusted by the non-adiabatic solution of the drift-kinetic equation. Here, ω and $k_\parallel$ is the mode characteristic frequency and parallel wavenumber, respectively, and v_e is the electron thermal velocity. In the hybrid model, the electron continuity equation is solved, in addition to the ion gyro-kinetic and electron drift-kinetic equations. The perturbed electrostatic potential ϕ and parallel vector potential $A_\parallel$ are calculated using gyrokinetic Poisson's equation and Faraday's law, respectively. The compressional component of perturbed magnetic field is neglected. The fluid-kinetic hybrid electron model has been successfully verified for ion-temperature-gradient (ITG) instability, trapped-electron mode (TEM), and KBM [16, 17], various Alfvén eigenmodes [18, 19], as well as kink [20] and tearing modes [21]. The hybrid approach is different from the kinetic closure approach [22, 23], which has failed to simulate microturbulence and Alfvén eigenmodes. The main difference between these two models is that the kinetic closure model uses the solution of exact electron drift-kinetic equation to calculate current. This method suffers from the well-known numerical difficulty of resolving tearing parity in mode rational surface. The fluid kinetic approximation explicitly removes tearing parity by solving Faraday's law for perturbed vector potential, and calculate electron current from the Ampére's law.

As in our previous studies [9] of the DIII-D pedestal instabilities, we consider two separate radial locations. It is found that KBM is marginally dominant in the steep gradient region. In the pedestal top region the dominant instability is ion temperature gradient mode. Linear properties of the observed modes are analyzed. The simulation results reported in this paper are still rather qualitative, since we ignore collisions and equilibrium flows, that would affect the observed instabilities. We have also suppressed the equilibrium current drive, which may destabilize the kink mode. The original intent of this research is to identify the stability domain of various modes as a function of local pressure profile, taking into account kinetic effects and realistic magnetic geometry. This and previous work [9] are important parts of GTC validation and verification efforts.

2. GTC simulation of DIII-D pedestal

To clarify the local drift-wave instability, we perform non-local simulation of the toroidal annulus $\psi_N = 0.90$–1.00 which includes the whole pedestal, while considering the gradients from two different locations within the pedestal (figure 1). To achieve this, we construct artificial pressure profiles to get constant gradient values of $d\ln(n,T)/d\psi_N$ from the pedestal top region ($\psi_N = 0.95$) and the steep gradients region ($\psi_N = 0.98$) throughout radial simulation domain. Here, ψ_N is the poloidal magnetic flux normalized by its value at the separatrix.

The constant gradient profiles are used to compare with local simulations and to address instabilities as function of
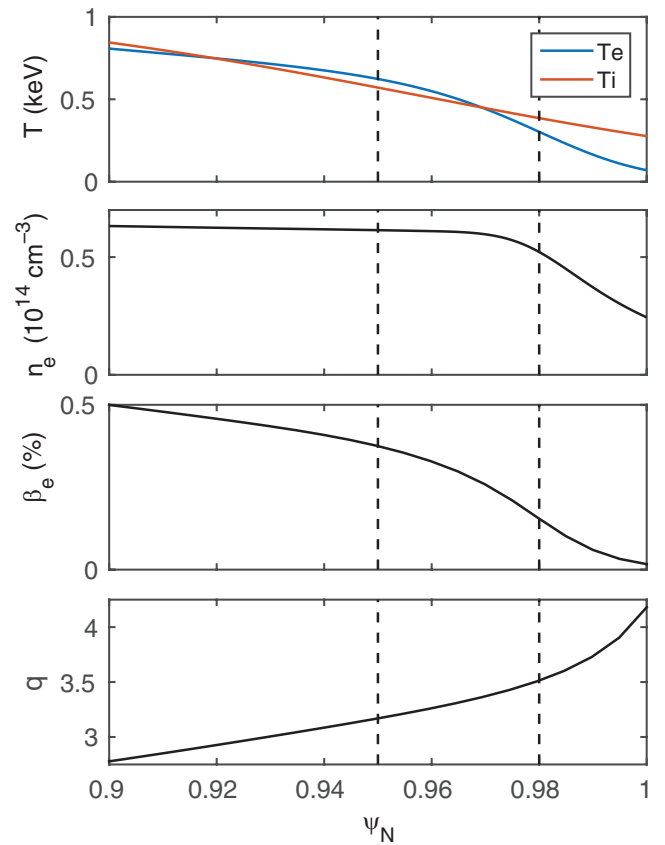

Figure 1. Equilibrium temperature, density, β_e and q profiles in the pedestal region of DIII-D discharge #131997 at time 3011 ms.
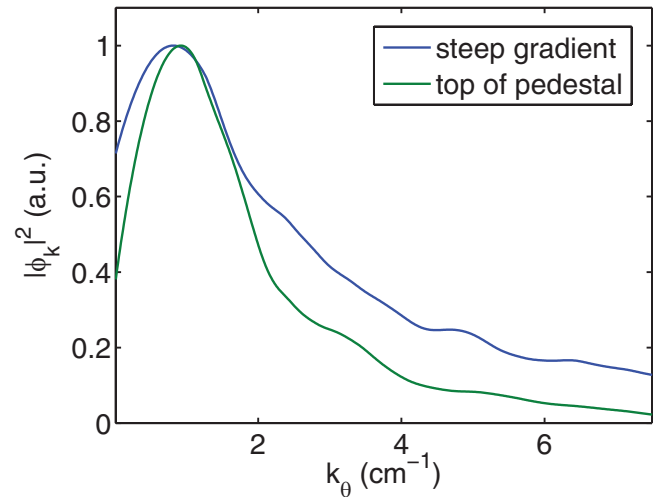

Figure 2. Poloidal spectrum of electrostatic fluctuations at the nonlinearly saturated stage in GTC electrostatic simulations.

pressure gradient. If the full profile would be used without equilibrium flow shear suppression effect, the steep gradient region instability would certainly dominate, due to much stronger drive there. Fixed boundary conditions are applied for all fluctuating quantities at both sides of radial simulation domain. The boundary conditions do not significantly affect the radial wavelength of the mode within simulation domain, which has been tested by moving inner boundary, although the growth rate may change if we allow mode to localize further
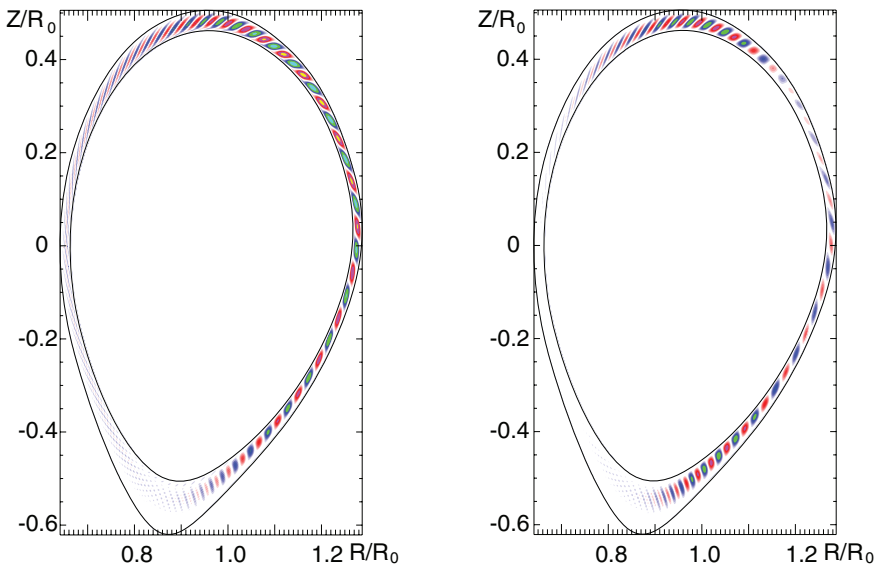
Figure 3. Poloidal snapshot of the $n = 20$ electrostatic potential (right panel) and parallel vector potential (left panel) fluctuations (equilibrium parameters from the peak gradient region, $\beta_e = 0.15\%$) in GTC electromagnetic simulations.
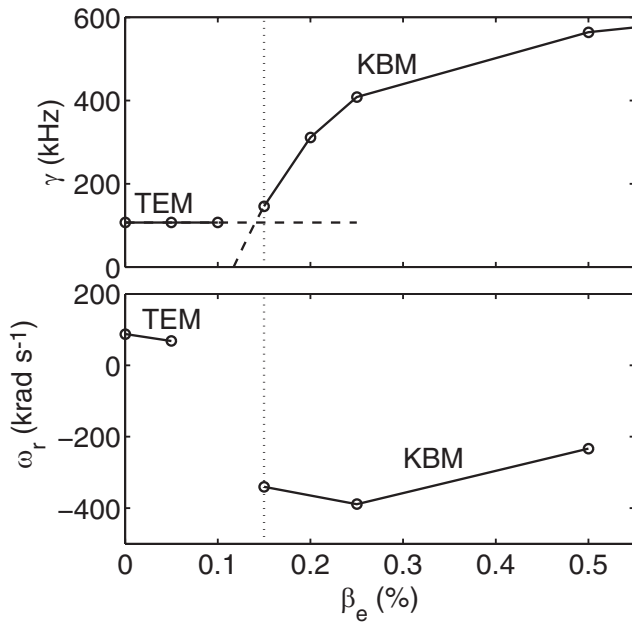

Figure 4. β_e dependence of the linear growth rate (top panel) and real frequency (bottom panel) of $n = 20$ instability in the peak gradient region from GTC simulation. Vertical dotted line indicates the experimental value of β_e.
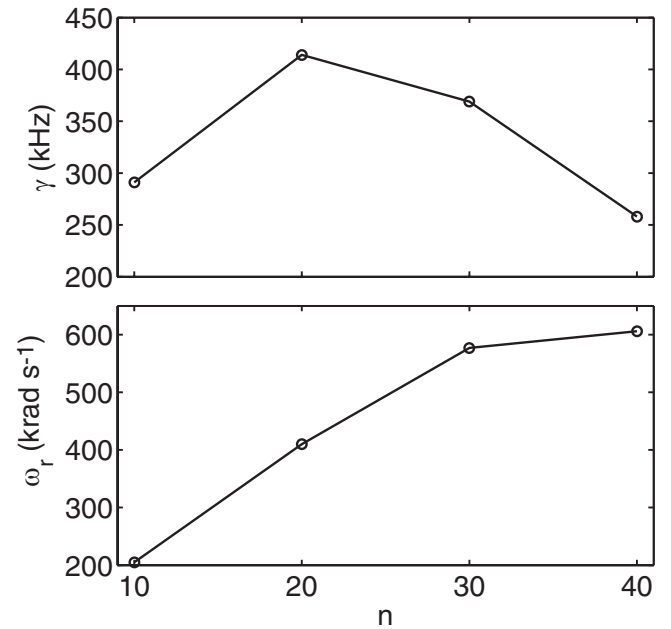

Figure 5. Toroidal mode number dependence of KBM growth rate (upper panel) and real frequency (lower panel) at the maximum gradient region with artificially increased $\beta_e = 0.25\%$ (from GTC simulation).

inward, where magnetic shear is smaller, while assuming constant drive. The proposed approach is not fully self consistent, but it allows to understand local linear instabilities dependent on the pressure gradients before moving towards more realistic simulations.

In the current work, linear simulations were performed with filtering modes of a single toroidal mode number n, picked either as the fastest growing mode or the dominant mode in the nonlinearly saturated state. For pedestal simulations we use 60 radial grid points, 32 toroidal and up to 2400 poloidal grid points. Grid, particle and temporal resolution has been tested for convergence.

In the previous electrostatic studies [9] at the maximum gradient region, we observe trapped electron mode as dominant instability, having the growth rate increasing monotonically with the toroidal mode number n, since there is no corresponding linear stabilization mechanism at high-n. At the top of the pedestal the dominant electrostatic instability is the ITG mode. To identify the relevant mode number we run the nonlinear electrostatic simulation including all modes. Looking at the fluctuation spectrum at saturated state (figure 2) we see that the maximum intensity is at $k_\theta \approx 1\,\mathrm{cm}^{-1}$ for both peak gradient and pedestal top regions, which corresponds to $m \approx 60$ and $n \approx m/q \approx 20$, where m is the poloidal mode number.
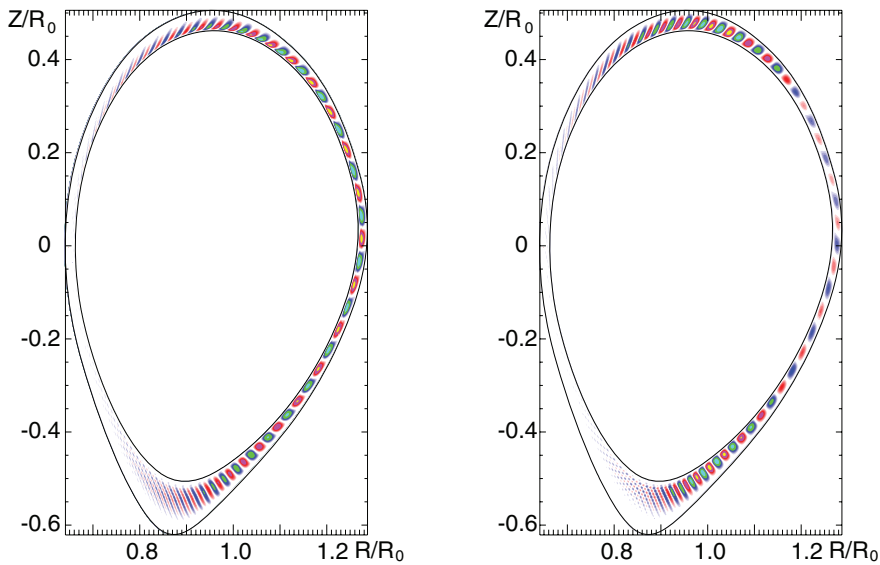
Figure 6. Poloidal snapshot of the $n = 20$ electrostatic potential (right panel) and parallel vector potential (left panel) fluctuations (equilibrium parameters from the pedestal top region, $\beta_e = 0.37\%$) in GTC simulation.
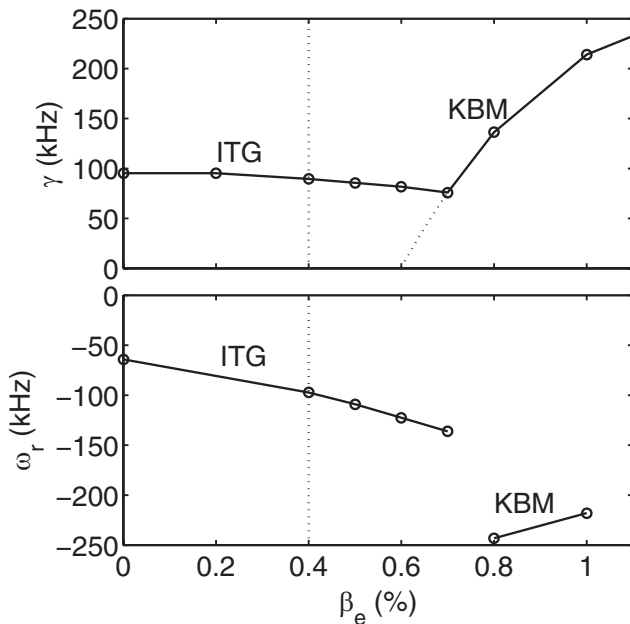

Figure 7. β_e dependence of the linear growth rate (top panel) and real frequency (bottom panel) of $n = 20$ instability in the pedestal top region in GTC simulation. Vertical dotted line indicates the experimental value of β_e.

We begin our electromagnetic studies by focusing at the maximum gradient region, characterized by strong electron pressure gradient ($R_0/L_{Te} \approx 120$, $R_0/L_{ne} \approx 60$), relatively weaker ion pressure gradient ($R_0/L_{Ti} \approx 50$, $n_i = n_e$), and $\beta_e \approx 0.15\%$, where $\beta_e \equiv 8\pi n_e T_e/B_0^2$. The linear electromagnetic simulation of $n = 20$ mode with local density and temperature taken at $\psi_N = 0.98$ recovers instability with the ballooning mode structure rotating in the ion diamagnetic direction (figure 3). The instability is insensitive to kinetic electron effects (instability is observed even when electrons are treated as a massless fluid), unlike the electrostatic TEM.

We further investigate the properties of observed instability for the dependence on β_e by changing electron density while keeping the gradient $d \ln n_e/d\psi_N$ unchanged. The dependence of linear growth rate and real frequency on β_e is shown in the figure 4, where vertical dotted line indicates experimental β_e-value. As we can see, at low β_e the growth rate remains approximately constant at electrostatic value, which corresponds to the trapped electron mode (positive real frequency). At $\beta_e \gtrsim 0.14\%$ the KBM instability takes over. From the top panel of figure 4 the KBM stability threshold can be extrapolated at $\beta_e \approx 0.12\%$ which is slightly below experimental value of $\beta_e = 0.15\%$ at $\psi_N = 0.98$. (figure 1, bottom panel). Unlike the growth rate, the real frequency of TEM mode decreases with β_e (figure 4, bottom panel), such that mode becomes more of the interchange type. This can be explained by the reduction of parallel electric field due to the increased inductive component that partially cancels the electrostatic component.

To address the dispersion properties of KBM we plot the dependence of the linear growth rate and real frequency on the toroidal mode number (figure 5). We have slightly increased the β_e value to 0.25% to stay away from the TEM–KBM transition point, to make sure we are dealing with clear KBM mode. As we can see, the KBM growth rate is peaked at $n \approx 20$, which is in agreement with experimental observations [4]. Thus our choice of $n = 20$ as a relevant toroidal mode number is justified for both electrostatic end electromagnetic simulations.

Since KBM is linearly stabilized at higher toroidal mode number, while the TEM growth rate increases monotonically with n, the TEM–KBM transition occurs at higher β_e for higher toroidal mode numbers. In fact, for $n = 60$ the transition occurs at $\beta_e \approx 0.2\%$, and KBM becomes subdominant at the experimental value of pressure. Thus, to get a complete picture of relevant instabilities, one needs to go beyond linear analysis and to take into account nonlinear saturation mechanisms.

Finally, we consider the pedestal top region ($\psi_N = 0.95$), which is characterized by weak gradients of density and electron temperature ($R_0/L_{ne} \approx 2$, $R_0/L_{Te} \approx 25$), and relatively stronger ion temperature gradient ($R_0/L_{Ti} \approx 30$). Linear electromagnetic simulations recover unstable mode with extended ballooning structure (figure 6), rotating in the ion diamagnetic direction. To identify the observed mode we have varied the β_e value by changing the electron density. The linear growth rate and real frequency dependence on β_e are shown in figure 7. At the top panel of figure 7 we see the familiar β-stabilization of ITG mode and the onset of KBM, similar to our results reported in [16]. The KBM becomes dominant at $\beta_e > 0.7\%$, with the estimated instability threshold at $\beta_e \approx 0.6\%$. As we can see, the experimental value of $\beta_e \approx 0.4\%$ at $\psi_N = 0.95$ corresponds to the electromagnetic ITG branch.

3. Conclusions

We have done non-local gyrokinetic simulations using realistic equilibrium and profiles of H-mode pedestal in DIII-D discharge #131997 at time 3011 ms. Two radial locations are considered : steep gradient region and pedestal top region. The dominant instability in the pedestal top region is identified as finite-β ion-temperature gradient mode. In the steep gradient region the kinetic ballooning mode is dominant for $k_\theta \sim 1$ cm^{-1} range, corresponding to the maximum KBM growth rate. By artificially varying plasma pressure we observe the transition from ITG to KBM branch at the pedestal top region, and transition from TEM to KBM branch in the steep gradient region. Due to the lack of linear TEM stabilization mechanism for high n, the transition from TEM to KBM occurs at higher pressure for short wavelength modes.

Acknowledgment

References

[1] Snyder P.B. *et al* 2009 *Nucl. Fusion* **49** 085035
[2] Snyder P.B., Groebner R.J., Leonard A.W., Osborne T.H. and Wilson H.R. 2009 *Phys. Plasmas* **16** 056118
[3] Evans T.E. *et al* 2006 *Nat. Phys.* **2** 419
[4] Yan Z., McKee G.R., Groebner R.J., Snyder P.B., Osborne T.H. and Burrell K.H. 2011 *Phys. Rev. Lett.* **107** 055004
[5] Wang E., Xu X., Candy J., Groebner R.J., Snyder P.B., Chen Y., Parker S.E., Wan W., Lu G. and Dong J.Q. 2012 *Nucl. Fusion* **52** 103015
[6] Wan W., Parker S.E., Chen Y., Yan Z., Groebner R.J. and Snyder P. 2012 *Phys. Rev. Lett.* **109** 185004
[7] Groebner R.J. 2013 *Nucl. Fusion* **53** 093024
[8] Dickinson D., Roach C.M., Saarelma S., Scannell R., Kirk A. and Wilson H.R. 2012 *Phys. Rev. Lett.* **108** 135002
[9] Fulton D., Lin Z., Holod I. and Xiao Y. 2014 *Phys. Plasmas* **21** 042110
[10] Lin Z., Hahm T.S., Lee W.W., Tang W.M. and White R.B. 1998 *Science* **281** 1835
[11] Xiao Y., Holod I., Wang Z.X., Lin Z. and Zhang T.G. 2015 *Phys. Plasmas* **22** 022516
[12] Lao L.L., Stjohn H., Stambaugh R.D., Kellman A.G. and Pfeiffer W. 1985 *Nucl. Fusion* **25** 1611
[13] Hirshman S.P. and Whitson J.C. 1983 *Phys. Fluids* **26** 3553
[14] Groebner R.J., Leonard A.W., Snyder P.B., Osborne T.H., Maggi C.F., Fenstermacher M.E., Petty C.C. and Owen L.W. 2009 *Nucl. Fusion* **49** 085037
[15] Holod I., Zhang W.L., Xiao Y. and Lin Z. 2009 *Phys. Plasmas* **16** 122307
[16] Holod I. and Lin Z. 2013 *Phys. Plasmas* **20** 032309
[17] Deng W., Lin Z. and Holod I. 2012 *Nucl. Fusion* **52** 023005
[18] Zhang H.S., Lin Z. and Holod I. 2012 *Phys. Rev. Lett.* **109** 025001
[19] Wang Z.X., Lin Z., Holod I., Heidbrink W.W., Tobias B., Van Zeeland M. and Austin M.E. 2013 *Phys. Rev. Lett.* **111** 145003
[20] McClenaghan J., Lin Z., Holod I., Deng W. and Wang Z. 2014 *Phys. Plasmas* **21** 122519
[21] Liu D.J., Zhang W.L., McClenaghan J., Wang J. and Lin Z. 2014 *Phys. Plasmas* **21** 122520
[22] Cohen B.I., Dimits A.M., Nevins W., Chen Y. and Parker S.E. 2002 *Phys. Plasmas* **9** 251
[23] Chen Y., Parker S.E., Wan W. and Bravenec R. 2013 *Phys. Plasmas* **20** 092511